Ultrahigh thermoelectric performance in $Cu_{2-y}Se_{0.5}S_{0.5}$ liquid-like materials

Kunpeng Zhao[a,b], Pengfei Qiu[a], Qingfeng Song[a,b],Anders Bank Blichfeld[c,d], Espen Eikeland[c], Dudi Ren[a], Binghui Ge[e], Bo B. Iversen[c], Xun Shi[a]*, and Lidong Chen[a]*

[a] State Key Laboratory of High Performance Ceramics and Superfine Microstructure, Shanghai Institute of Ceramics, Chinese Academy of Science, Shanghai 200050, China.

[b] University of Chinese Academy of Sciences, Beijing 100049, China.

[c] Centre for Materials Crystallography, Department of Chemistry and iNANO, Aarhus University, Langelandsgade 140, DK-8000 Aarhus C, Denmark.

[d] Department of Materials Science and Engineering, Norwegian University of Science and Technology, N-7491 Trondheim, Norway.

[e] Beijing National Laboratory for Condensed Matter Physics, Institute of Physics, Chinese Academy of Science, Beijing 100190, China.

* Corresponding author. E-mail: xshi@mail.sic.ac.cn and cld@mail.sic.ac.cn

Abstract

Liquid-like thermoelectric materials have recently received heightened attentions due to their exceptional thermal and electrical transport properties. As a typical example, $Cu_{2-y}Se$ has good electrical transport properties while $Cu_{2-y}S$ has extremely low lattice

thermal conductivity. Combining these stirring characters into one material is expected to result in excellent thermoelectric performance. In this study, we found that $Cu_{2-y}Se$ and $Cu_{2-y}S$ can form a solid solution in the composition range down to half Se and half S. XRD, SEM and TEM reveal that $Cu_{2-y}Se_{0.5}S_{0.5}$ possesses a unique hierarchical microstructure composed of mesoscale polymorphs, nanoscale domains and modulations. Besides, the liquid-like copper ions at high temperature not only strongly scatter lattice phonons but also eliminate some of the transverse phonon vibrations. Combining with the extraordinarily low sound speeds, an overall ultralow thermal conductivity is achieved in $Cu_{2-y}Se_{0.5}S_{0.5}$ with the values similar to that in Cu_2S. Furthermore, the electrical transport performance of $Cu_{2-y}Se_{0.5}S_{0.5}$ is significantly improved through tuning its native Cu vacancies. High electrical power factors similar to or even superior to $Cu_{2-y}Se$ are observed due to the high weighted mobility. All these favorable factors lead to much enhanced quality factor and thus remarkably high thermoelectric performance in $Cu_{2-y}Se_{0.5}S_{0.5}$, which reaches a *ZT* of 2.3 at 1000 K, among the highest values in bulk materials.

Keyword: thermoelectric, quality factor, liquid-like, thermal conductivity, electrical conductivity

1. Introduction

Thermoelectric (TE) materials have attracted worldwide renewed interests as concerns with the more efficient use of energy resources and minimization of

environmental damage [1-9]. Thermoelectric materials and devices are heat engines that either use electricity to pump heat from a cold side to a hot reservoir or convert industrial waste heat into useful electricity [10, 11]. At the material level in the field of thermoelectrics, the overriding goal is to maximize the thermoelectric Figure of merit ZT ($= S^2T/(\rho\kappa)$), where S is the Seebeck coefficient (also called thermopower), T is the absolute temperature, ρ is the electrical resistivity, and κ is the thermal conductivity. The challenge to obtain high ZT thermoelectric materials lies in achieving simultaneously high S, low ρ and low κ in one material because these three parameters are strongly correlated and highly dependent on each other.

Recently, the concept of "Phonon-Liquid Electron-Crystal" (PLEC) has been proposed to explain the extraordinarily low thermal conductivity and high thermoelectric performance in copper (or silver)-based superionic conductors [12-15]. Along this direction, many novel superionic TE materials have been discovered with superior TE properties with the typical examples of binary compound $Cu_{2-y}Se$, Ag_2Se and ternary compound Cu_5FeS_4 and Cu_7PSe_6 [12, 16-18]. In particular, binary copper chalcogenides $Cu_{2-y}X$ (X=Se, S or Te) have stimulated keen interest in the past few years due to their exceptional and abnormal thermal and electrical transport properties. An ultralow lattice thermal conductivity (κ_L) down to 0.33 W m^{-1} K^{-1} is observed in the simple binary compound $Cu_{2-y}X$ [13, 19], leading to very high ZTs of 1.7-1.9 in Cu_2S [13, 20], 1.5-1.8 in Cu_2Se [12, 21-24], and 1.1 in Cu_2Te [25], which are among the best values in bulk TE materials. The materials are p-type self-doped materials with the carrier concentrations determined by the concentration of native Cu

vacancies. Although the chemical formula is very simple, the crystal structures are quite complex. At room temperature, $Cu_{2-y}X$ is a normal solid state compound with ordered copper ions in the crystal lattice [26]. Upon heating, copper chalcogenides $Cu_{2-y}X$ experience phase transitions with the transition temperatures dependent on the exact chemical compositions [27-29]. At high temperature they transform into superionic conductors with an anti-fluorite cubic structure at high temperatures. The anion X^{2-} form a rigid framework that provides a crystalline pathway for electron transport (called the solid sublattice). On the other hand, the Cu^{+} ions are kinetically distributed over multiple sites with a mobility like a liquid (called liquid sublattice). These liquid-like ions not only scatter heat-carrying phonons but also eliminate some of the transverse vibrational modes, leading to the specific heat per volume (C_v) below the Dulong-Petit value at high temperatures [12]. Furthermore, it is very surprising that, in spite of the large atomic size difference between S and Te, Cu_2S and Cu_2Te can form a complete solid solution with a very special mosaic crystal microstructure, leading to simultaneously improving the Seebeck coefficient and reducing the lattice thermal conductivity κ_L. Thus an ultrahigh ZT value of 2.1 is observed in $Cu_2S_{0.52}Te_{0.48}$ with the composition composed of around half-S and half-Te [30]. The atomic size and electronegativity of the element Se are more closely resembling S than Te. Therefore, Cu_2Se and Cu_2S are expected to more easily form solid solutions. In addition, the electrical transport properties of $Cu_{2-y}Se$ are superior to that of $Cu_{2-y}S$ and $Cu_{2-y}Te$ due to its large weighted mobility and optimum hole concentrations while $Cu_{2-y}S$ has extremely low lattice thermal conductivity [13]. Thus

the solid solutions of $Cu_{2-y}Se_{0.5}S_{0.5}$ with half-S and half-Se may possess the good electrical transport properties stemming from Cu_2Se and the low lattice thermal conductivity of Cu_2S, and thereby reaching an outstanding *ZT* value. In this work, we demonstrate that the $Cu_{2-y}Se_{0.5}S_{0.5}$ compounds are thermodynamically stable with very complex hierarchical microstructures, good electrical transport, ultralow lattice thermal conductivity leading to a remarkably high *ZT* value of 2.3 at 1000 K.

2. Experimental Section

Synthesis. Polycrystalline $Cu_{2-y}Se_{0.5}S_{0.5}$ (x = 0, 0.03, 0.04, 0.05, 0.06, and 0.15) samples were prepared by melting Cu (shot, 99.999%, Alfa Aesar), Se (shot, 99.999%, Alfa Aesar), and S (shots, 99.9999%, Alfa Aesar) in Pyrolytic Boron Nitride (P-BN) crucibles enclosed in fused silica tubes under vacuum. The tubes were slowly (100 K h^{-1}) raised to 1423 K and dwelled for 12 h, and then cooled down to 1073 K in 24 h. After annealing at 1073 K for 8 days, the tubes were furnace cooled to room temperature. Small single crystals were extracted from the polycrystalline ingot sample after the annealing process. Finally, the annealed ingots were crushed into powders and consolidated by spark plasma sintering (Sumitomo SPS-2040) at 873 K under a pressure of 65 MPa for 5 minutes. Electrically insulating and thermally conducting BN layers were sprayed onto the surface of carbon foils and the inner sides of the graphite die before the SPS process in order to prohibit DC pulsed currents going through the powders.

Characterization. Single-crystal (about 10 × 40 × 60 μm^3) X-ray diffraction

(SCXRD) measurements were performed on a SuperNova diffractometer from Agilent Technologies using $Mo_{K\alpha}$ radiation (λ= 0.71073 Å). Diffracted intensities were collected on a CCD detector and the data were integrated and corrected for absorption using CrysAlisPro. The structure solution and refinement were carried out with SHELXT, using the Olex2 gui. Room-temperature powder X-ray diffraction (RT-PXRD) measurements were carried out on Rigaku Rint 2000 with a Cu-K_α source. High-temperature powder X-ray diffraction (HT-PXRD) data of $Cu_2Se_{0.5}S_{0.5}$ were collected at the beam line BL44B2 at SPring-8, Japan (λ = 0.500378(5) Å) [31]. The sample morphologies were measured by field emission scanning electron microscopy (FESEM, Magellan-400) equipped with energy dispersive X-ray analysis (EDS, Horiba 250). The TEM examination was performed on a JEM-2100F field-emission transmission electron microscope. The photoelectron spectra (XPS) were measured on pressed pellets by using a Thermo Fisher Scientific ESCALAB 250 with monochromatic Al K_α X-ray (1486.74 eV). The carbon 1s peak was used as a reference to calibrate the binding energies of the other core level spectra. The sound speed data were obtained by use of ultrasonic measurement system UMS-100 with shear wave transducers of 5 MHz and longitudinal wave transducers of 10 MHz. The electrical resistivity (ρ) and Seebeck coefficient (S) were simultaneously obtained on a commercial system (ULVAC ZEM-3). Thermal diffusivity (D) was measured using the laser flash method (Netzsch, LFA-457). The specific heat (C_p) was determined by differential scanning calorimetric using Netzsch DSC 404F3. The densities (d) were measured by the Archimedes method. The total thermal conductivity (κ) was

calculated according to the relationship $\kappa = dC_pD$. Uncertainties in the electrical conductivity, Seebeck coefficient, and thermal conductivity were within 5%, 7%, and 5%, respectively. The Hall coefficient (R_H) at 300 K was measured using a physical properties measurement system (PPMS-9, Quantum Design, USA) with a magnetic field from -3 to 3 T. The hole concentration (p) was calculated using $p = 1/(R_He)$, where e is the elementary charge. Hall carrier mobility (μ_H) was calculated according to the relation $\mu_H = R_H/\rho$.

3. Results and Discussion

Single-crystal X-ray diffraction is used to determine the crystal structure of $Cu_2Se_{0.5}S_{0.5}$ at 100 K. Small single crystals with the size of about 10 × 40 × 60 μm^3 were extracted from a polycrystalline ingot cooled from high temperature after a long time element melting. The detailed crystallographic information is listed in Table S1. Different from the room temperature structures for Cu_2Se [26] and Cu_2S [28], we found that the $Cu_2Se_{0.5}S_{0.5}$ has a hexagonal structure with the space group of $P6_3/mmc$, which is the same as the intermediate temperature phase of Cu_2S. The solved crystal structure of $Cu_2Se_{0.5}S_{0.5}$ is shown in Fig. 1a. It consists of a Se/S atomic site and two disordered copper sites (Cu1 & Cu2). The Se/S atoms form a rigid hexagonal framework. The disordered Cu1 site is situated on the faces of the red octahedron shown in Fig. 1a. The Cu2 site is disordered about the 6_3-screw axis, split into three equivalent positions located in the blue tetrahedron. The Se/S sites are fully occupied by half Se and half S, while the Cu1 and Cu2 sites are partially occupied with the site

occupancy factors (S.O.F.s) of 0.550 and 0.172, respectively. This type of disordered Cu atoms is the typical character of superionic semiconductors [14, 32], in which Cu ions can easily migrate among these partially occupied atomic sites.

The room temperature powder X-ray diffraction (PXRD) data are consistent with the single crystal structural solution. As shown in Fig. 1b and Fig. S1, most of the diffraction peaks of $Cu_2Se_{0.5}S_{0.5}$ can be clearly indexed to the hexagonal structure described above, with the exception of some weak peaks that are identified as the $Fm\bar{3}m$ cubic structure (ICSD-54916), indicating mixed hexagonal and cubic phases in $Cu_2Se_{0.5}S_{0.5}$. This is consistent with the presence of different polymorphs of materials [33, 34]. With increasing copper vacancies, the intensities of diffraction peaks belonging to the cubic phase are increased. When the copper vacancy level reaches 0.15 (y = 0.15), only the cubic phase is observed in the XRD patterns without any other secondary phases. Such phase evolution induced by the change of copper-deficiency is also observed for $Cu_{2-y}Se$ and $Cu_{2-y}S$ [35, 36].

In order to further characterize the structural phase transitions, synchrotron powder diffraction data were collected in the temperature range from 300 to 1000 K. As shown in Fig. 1c, all the reflections from hexagonal phase disappear and only the peaks from cubic phase are observed above 700 K, which is consistent with the DSC measurements shown in Fig. S2. It is very interesting to note that above 400 K, the intensities of the diffraction peaks belonging to the cubic phase are gradually increased, while those from the hexagonal phase are gradually reduced. Therefore, the phase transition from the hexagonal phase to the cubic phase continuously occurs

from the low temperatures around 400 K and finishes at about 700 K. Such a broad temperature range phase transition introduces extra enthalpy into the DSC measurement, leading to a relatively large heat capacity as compared with the data above 700 K (see Fig. S2). In addition, we calculated the energy difference between the hexagonal phase and cubic phase based on the DSC measurement, and found that it is about 7.56 J g^{-1}. Such small energy deviation can easily lead to the formation of polymorph phases shown above induced by thermal fluctuations. Furthermore, thermal fluctuation also results in the slow growth of the cubic phase of $Cu_2Se_{0.5}S_{0.5}$ when $T \geqslant 400$ K and finally a complete transition is observed near 700 K. Such a phase transformation mechanism are observed in many chalcogenides such as Cu_4SeTe and ZnS [37, 38].

The material phases and element distributions are investigated by using electron backscatter diffraction (EBSD) on the $Cu_{1.94}Se_{0.5}S_{0.5}$ sample. The EBSD measurements clearly show the co-existence of the hexagonal phase (red grains shown in Fig. 2a) and cubic phase (blue grains shown in Fig. 2a) at room temperature. The in-situ energy dispersive spectroscopy (EDS) mapping (Fig. 2c) shows that all elements are homogeneously distributed, implying the chemical compositions of hexagonal phase and cubic phase are very close or identical. This completely agrees with the definition of polymorphism, *e.g.*, a material with different crystal structures but same chemical composition. The grain sizes of hexagonal and cubic phases calculated from the phase map (shown in Fig. 2a) are shown in Fig. 2b with the value ranging from 150 nm to 5 μm. Here the sampling step size is 60 nm. We took the

value of two-and-a-half times of the step size as the minimum grain size (150 nm). Thus the pixel clusters below 150 nm are regarded as noise. The grains below 150 nm are thus ignored and is the limiting size for detection by EBSD. Besides, EBSD orientation maps show that the $Cu_{1.94}Se_{0.5}S_{0.5}$ sample has a randomly oriented texture structure as shown in Fig. S3. Hence, it can be regarded as an isotropic sample.

We carried out transmission electron microscopy (TEM) analysis on samples of $Cu_2Se_{0.5}S_{0.5}$ and $Cu_{1.94}Se_{0.5}S_{0.5}$. As shown in Fig. 3a, the low-magnification TEM image and selected area electron diffraction (SAED) pattern clearly show hexagonal structure in $Cu_2Se_{0.5}S_{0.5}$. However, high angle annular dark field (HAADF) images shown in Fig. 3c and 3f clearly visualize the hexagonal and cubic polymorphs of $Cu_2Se_{0.5}S_{0.5}$ and $Cu_{1.94}Se_{0.5}S_{0.5}$, being consistent with the XRD and EBSD observations shown in Fig. 1 and 2. In addition, beyond the machine limitation of EBSD technique, the high-resolution TEM images shown in Fig. 3b and Fig. S4 demonstrate the crystallized region actually contains plenty of domains with the sizes about 20-80 nm. The SAED patterns shown in Fig. 3d and the HAADF image shown in Fig. 3e indicate that, beyond the primitive cubic phase, a modulated cubic phase also exist in the $Cu_{1.94}Se_{0.5}S_{0.5}$ sample. Based on the Fourier filtered images shown in Fig. S5, the modulation is believed to be caused by the disordered copper rather than selenium. It should be noted that the nano-domains, modulation, as well as polymorph could be beneficial for heat impedance.

The temperature dependence of thermoelectric properties for $Cu_{2-y}Se_{0.5}S_{0.5}$ (y = 0, 0.03, 0.04, 0.05, and 0.06) is shown in Fig. 4, which covers the low-temperature

mixed phases (hexagonal+cubic) and high-temperature cubic phase. All the $Cu_{2-y}Se_{0.5}S_{0.5}$ samples show obviously two different temperature dependencies in the temperature range from 300 K to 1000 K studied here due to the phase transition. Because of the natural deficiency of copper, all samples including nominal-stoichiometric $Cu_2Se_{0.5}S_{0.5}$ show p-type conducting behavior. The room temperature resistivity ρ for $Cu_2Se_{0.5}S_{0.5}$ is on the order of 10^{-2} Ω m, which is higher than that in Cu_2Se and Cu_2S. At temperatures above 700 K, the resistivity is reduced by about two orders of magnitude and finally to 3×10^{-4} Ω m at 1000 K. The room temperature Seebeck coefficient (S) of $Cu_2Se_{0.5}S_{0.5}$ is around 490 μV K^{-1}. At first, it decreases monotonously to about 340 μV K^{-1} at 700 K and then it increases to 370 μV K^{-1} at 1000 K, lying between the Seebeck coefficient of Cu_2Se (= 294 μV K^{-1}) and Cu_2S (= 438 μV K^{-1}). With increasing copper deficiency from $Cu_2Se_{0.5}S_{0.5}$ to $Cu_{1.94}Se_{0.5}S_{0.5}$, both ρ and S are significantly reduced in the whole temperature range due to the increased hole concentrations, which will be discussed later. The rapid change in ρ and S for $Cu_2Se_{0.5}S_{0.5}$ around 650 K is attributed to the structural transition from the mixed phases (hexagonal+cubic) to single cubic phase. We also found that the phase transition temperature is decreased with increasing copper deficiency, which is consistent with the DSC measurements shown in Fig. S2. Based on the measured ρ and S, the calculated power factors ($PF = S^2/\rho$) for $Cu_{2-y}Se_{0.5}S_{0.5}$ are shown in Fig. 4c. Clearly, the PFs gradually increase with increasing copper deficiency with a largest PF of 13.2 μW cm^{-1} K^{-2} obtained at 1000 K. This is higher than that in Cu_2Se and Cu_2S matrix compound. We ran the repeatability measurement

up to 1000 K for sample $Cu_{1.94}Se_{0.5}S_{0.5}$ and the data are shown in Fig. S6 and S7. The electrical conductivity and Seebeck coefficient are nearly reproducible above the phase transition temperatures (around 600 K). Besides, a transformation hysteresis is observed below 600 K after a heating and cooling cycle, which is attributed to the material's phase transitions.

Fig. 4d presents the temperature dependence of total thermal conductivity κ for $Cu_{2-y}Se_{0.5}S_{0.5}$. In the whole temperature range, the values of the total thermal conductivity for all $Cu_{2-y}Se_{0.5}S_{0.5}$ (y = 0, 0.03, 0.04, 0.05, and 0.06) samples are below 1.1 W m^{-1} K^{-1}. These are remarkably low values even in TE materials. Different from ρ or S, all samples show an enhanced κ when increasing the copper deficiency. This is mainly a result of the reduced electrical resistivity and thus enhanced electrical thermal conductivity. The lattice thermal conductivity (κ_L) is calculated using the expression $\kappa_L = \kappa - \kappa_c$, in which the charge carrier thermal conductivity component (κ_c) is estimated using the Wiedemann-Franz law ($\kappa_c = LT/\rho$, where L is the Lorenz number). In this study, the L values are obtained from the accepted approach of fitting the Seebeck data to the reduced chemical potential and the calculated values are shown in Fig. S8 [39, 40]. All the samples show a weak temperature dependent behavior in κ_L, which is a typical character of liquid-like materials [2, 12]. For high temperature cubic phases, the κ_L values of $Cu_{2-y}Se_{0.5}S_{0.5}$ samples are as low as 0.32 W m^{-1} K^{-1}, which is comparable to that of Cu_2S (= 0.33 W m^{-1} K^{-1}) but much lower than that in Cu_2Se (= 0.52 W m^{-1} K^{-1}) [12, 13].

Based on the measured ρ, S, and κ, the dimensionless TE Figure of merit ZT (=

$S^2T/(\rho\kappa)$) is calculated and shown in Fig. 4f. Similar to the electrical and thermal transport properties, the *ZT* values also show two different trends in the measured temperature range due to the phase transitions. The low temperature *ZT*s are for the mixed phases (hexagonal+cubic) and high temperature *ZT*s are for the single cubic phase. The *ZT* values for all samples below 550 K are no more than 0.3 due to the low electrical transport properties at low temperatures. The maximum *ZT* obtained for stoichiometric $Cu_2Se_{0.5}S_{0.5}$ is around 1.2 at 1000 K, in between the values of Cu_2Se (= 1.5 @ 1000 K) and Cu_2S (= 0.6 @ 1000 K). Clearly, the *ZT* values at high temperature are gradually increased with increasing copper vacancies, which is mainly attributed to the improved power factors. A remarkable high *ZT* value of 2.3 is achieved at 1000 K for $Cu_{1.94}Se_{0.5}S_{0.5}$, which is among the highest values in bulk TE materials and greater than the maximum *ZT*s in $Cu_{2-y}Se$ and $Cu_{2-y}S$.

To better understand the effect of copper vacancies on electrical transport properties, we measured the room temperature Hall coefficient for all samples. The relationship between the measured Hall carrier concentration (p) and copper vacancies y for $Cu_{2-y}Se_{0.5}S_{0.5}$ at 300 K is plotted in Fig. 5a. The data of $Cu_{2-y}Se$ and $Cu_{2-y}S$ are also included for comparison. It is clear that the exact stoichiometric composition ($Cu_2Se_{0.5}S_{0.5}$) is a nearly intrinsic semiconductor with low carrier concentration about 1.03×10^{18} cm^{-3}, which is lower than those of Cu_2Se and Cu_2S. With increasing copper deficiency from $Cu_2Se_{0.5}S_{0.5}$ to $Cu_{1.94}Se_{0.5}S_{0.5}$, the carrier concentration is significantly increased from the order of 10^{18} cm^{-3} to 10^{20} cm^{-3}. This significant increase in hole concentration is also observed in $Cu_{2-y}Se$ and $Cu_{2-y}S$ [12, 13]. The X-ray

photoelectron spectroscopy (XPS) measurements (see Fig. S9) indicate that the valence states of Cu, Se, and S are +1, -2 and -2, respectively. Thus the improved carrier concentration in these compounds can most likely be explained by the increase in Cu vacancies. Owing to the superionic character of $Cu_2Se_{0.5}S_{0.5,}$ the carrier mobility μ_H of $Cu_2Se_{0.5}S_{0.5}$ is only about 3 $cm^2 V^{-1} s^{-1}$, which is much lower than the μ_H in normal solid compound Cu_2Se and Cu_2S at room temperature. However, the μ_H of $Cu_{2-y}Se_{0.5}S_{0.5}$ shows a weak dependence when increasing copper vacancies, in contrast to the sharp decrease of μ_H in $Cu_{2-y}Se$ and $Cu_{2-y}S$. Even though the high temperature Hall coefficient is hard to measure, it can be deduced that the high temperature carrier mobility μ_H of $Cu_2Se_{0.5}S_{0.5}$ should be similar to those in Cu_2Se and Cu_2S (see Fig. S10). Due to the lower p and $\mu_{H,}$ the room temperature resistivity ρ of $Cu_2Se_{0.5}S_{0.5}$ is much higher than those in Cu_2Se and Cu_2S. With increasing copper deficiencies from $Cu_2Se_{0.5}S_{0.5}$ to $Cu_{1.94}Se_{0.5}S_{0.5}$, the ρ is significantly reduced by three orders of magnitude due to the improved carrier concentrations. The Seebeck coefficient S, as expected, exhibits the same decreasing trend with increasing copper deficiencies. The similar phenomena are also observed in binary $Cu_{2-y}Se$ and $Cu_{2-y}S$, indicating the high adjustability of electrical transport properties in copper chalcogenides.

To shed light on the origin of superior TE performance in $Cu_{2-x}Se_{0.5}S_{0.5}$ compared to its counterparts $Cu_{2-y}Se$ or $Cu_{2-y}S$, we modeled the electronic properties using a single parabolic band (SPB) model [41, 42]. Here the data for large copper deficient samples with carrier concentration $>10^{20}$ cm^{-3} are selected and used, thereby

it is reasonable to assume that the carrier concentration is scarcely changed from room temperature to high temperatures since they are degenerate semiconductors with large band gaps. Besides, the carrier mobility of $Cu_{2-y}Se$ or $Cu_{2-y}S$ are assumed to be limited by the acoustic phonon scattering while $Cu_{2-x}Se_{0.5}S_{0.5}$ is simultaneously dominated by both acoustic phonon and alloy scattering. All the estimated parameters including the effective mass m^*, the mobility parameter μ_0, the deformation potential Ξ, the alloy scattering potential U, the lattice thermal conductivity κ_L and the quality factor β are shown in Table 1. The Pisarenko relation, *i.e.*, a plot of S as a function of p, gives a good description for the experimental results. As shown in Fig. 6a, the data of $Cu_{2-x}Se_{0.5}S_{0.5}$ and $Cu_{2-y}Se$ samples fall on the same line with an effective mass m^* of 4.2 m_e (m_e is the mass of an electron), while the $Cu_{2-y}S$ samples possess a slightly higher effective mass. The corresponding mobility parameter μ_0 in $Cu_{2-y}S$ is smaller than the μ_0 in $Cu_{2-x}Se_{0.5}S_{0.5}$ and $Cu_{2-y}Se$ because $\mu_0 \propto 1/ m^*$. As a result, the calculated weighted mobility ($\mu_0(m^*/m_e)^{3/2}$) for $Cu_{2-y}Se_{0.5}S_{0.5}$, $Cu_{2-y}Se$, and $Cu_{2-y}S$ are 20.6, 18.9, and 13.6 $cm^2\ V^{-1}s^{-1}$, respectively, suggesting the electrical transport performance of $Cu_{2-y}Se_{0.5}S_{0.5}$ is much better than that of $Cu_{2-y}S$ and $Cu_{2-y}Se$. These data also explain why the calculated and measured PFs for $Cu_{2-y}Se_{0.5}S_{0.5}$ are greater than those of $Cu_{2-y}Se$ and $Cu_{2-y}S$, as shown in Fig. 4c and 6b.

The lattice thermal conductivity κ_L as a function of copper vacancy y is shown in Fig. 7a. At high temperature (1000 K), all the $Cu_{2-y}Se_{0.5}S_{0.5}$ compounds have a simple cubic structure, in which κ_L slightly decreases with rising copper vacancies. At room temperature (300 K), the κ_L for $Cu_2Se_{0.5}S_{0.5}$ presents an opposite trend, *i.e.*, κ_L

increases as the copper deficiencies increase. However, these deviations in κ_L are very small. When considering the measurement and calculation errors, it is hard to conclude the κ_L is obviously changed through variation of Cu vacancies in $Cu_2Se_{0.5}S_{0.5}$. Nevertheless, the κ_L values in $Cu_2Se_{0.5}S_{0.5}$ from room temperature to high temperatures are extremely small, *i.e.*, around 0.3-0.4 W m^{-1} K^{-1}.

We also measured the thermal conductivity at low temperatures between 2 and 300 K as shown in Fig. 7b. Very interestingly and surprisingly, similar to amorphous α-SiO_2, the $Cu_{2-y}Se_{0.5}S_{0.5}$ displays a glass-like heat conduction with the typical glass plateaus observed between 10 and 20 K (see Fig. 7b) [43, 44]. This stands in a stark contrast with the temperature dependence of thermal conductivity of Cu_2S which exhibits a strong "hump" shape that is normally observed in crystalline materials [30, 45, 46]. Note that the XRD data in Fig. 1 clearly show that our $Cu_{2-y}Se_{0.5}S_{0.5}$ materials are typical crystalline compounds that is completely different from a glass. The low-temperature glass-like thermal conductivity in $Cu_{2-y}Se_{0.5}S_{0.5}$ can be traced, in part, to its unusual micro/nano structure discussed above. Mesoscale grains, in form of polymorph, can be regarded as long-wavelength phonon scattering centers. On the other hand, the nano-domains and modulated structures in nanoscale are effective in scattering short-wavelength phonons. This unique hierarchical microstructure significantly diminishes heat conductions and thus leads to the glass-like exceptionally low lattice thermal conductivity observed in Fig. 7b.

In addition, the extremely low κ_L values in $Cu_{2-y}Se_{0.5}S_{0.5}$ compounds can be related to its low speed of sound. As presented in Fig. 7c, both the longitudinal v_l and

v_t transverse speeds of sound in $Cu_{2-y}Se_{0.5}S_{0.5}$ are remarkably lower than those in binary Cu_2Se and Cu_2S. The abnormal values of sound speeds could be associated with the different structure of $Cu_{2-y}Se_{0.5}S_{0.5}$ from Cu_2Se and Cu_2S, since the sound speeds are directly dominated by the chemical bonds [1]. Nevertheless, these ultralow longitudinal and transverse speeds of sound lead to an overall reduction in average speed of sound (both arithmetic and geometric averages) and thus remarkably low κ_L values in $Cu_2Se_{1-x}S_x$ according to $\kappa_L = v_{avg}\, C_V\, l/3$ (l is phonon mean free path).

The liquid-like behavior of Cu ions can also diminish part of the transverse phonons and thus lower the specific heat per volume (C_v) and κ_L. Similar to Cu_2Se or Cu_2S, the Se/S atoms in $Cu_{2-y}Se_{0.5}S_{0.5}$ form a rigid crystalline sublattice while the highly disordered Cu ions are weakly bonded inside the sublattice exhibiting the liquid-like behavior. These liquid-like ions not only strongly scatter phonons (lowering l) but also eliminate some of the transverse vibrations (reducing C_V). The heat capacity at constant volume C_v for liquids is [47]

$$C_v = \frac{d(K+U_l+U_t(\omega > \omega_0))}{dT} = \left[3 - \left(\frac{\omega_0}{\omega_D}\right)^3\right] Nk_B \qquad , (1)$$

where K, U_l, U_t, ω_0, and ω_D are the kinetic energy, potential energy of longitudinal vibrations, potential energy of transverse vibrations, cut-off frequency, and Debye frequency of transverse phonons, respectively. The theoretical top-limit (Dulong-Petit value) of C_v for a solid crystal in the high temperature range is $3Nk_B$ because all the vibrations contribute to C_v ($\omega_0 = 0$ in Equation 1). While for liquid materials, the

transverse phonons with frequency lower than ω_0 can no longer store elastic energy due to the long-range fluidity of liquid-state molecules or ions, leading to much lower C_v compared to that in solid. The liquid-like materials are in part-crystalline part-liquid state, resulting in a decreased C_v lying between the solids and liquids, as demonstrated by a few reports. The heat capacity at constant pressure C_p is given by [48]

$$C_p = C_{ph} + C_e + 9\alpha^2 BVT \quad .(2)$$

Here the first term C_{ph} is the excitation of the phonon modes, *i.e.*, C_v. The second term C_e is the carrier contribution to the specific heat. It is rather small and can be ignored safely. The third term $9\alpha^2 BVT$ is the contribution from volume change and can be calculated from the thermal expansion coefficient α, bulk elastic modulus B, and average volume per atom V. The measured α is 2.6×10^{-5} K^{-1} for the high temperature cubic phase (see Fig. S11). The bulk modulus B is calculated from the sound speed data with the details shown in Supplementary material. Then the evaluated C_v data, as well as the C_p data are plotted in Fig. 7d. It can be seen that the C_v and even C_p of $Cu_{2-y}Se_{0.5}S_{0.5}$ (y = 0, 0.03, and 0.06) are clearly decreased to below the Dulong-Petit value derived for solids. The decreased C_v and reduced l induced by the Cu ions, as well as the ultralow sound speeds, work together to contribute to the extremely low lattice thermal conductivity at high temperature for $Cu_{2-y}Se_{0.5}S_{0.5}$ compounds.

We took a constant κ_L value of 0.30, 0.51, and 0.31 W m^{-1} K^{-1} for $Cu_{2-y}Se_{0.5}S_{0.5}$,

$Cu_{2-y}Se$, and $Cu_{2-y}S$, respectively. By combing the *PFs* calculated shown above, the relationship between *ZT* ($= \frac{PF}{Lpe\mu T+k_L}$) and Hall carrier concentration is calculated by the SPB model [41, 42], as shown in Fig. 8. The experimental data are consistent with the calculated curve. The optimum carrier concentrations for the three systems are almost the same, but the maximum *ZT* for $Cu_{2-y}Se_{0.5}S_{0.5}$ is clearly larger than those in $Cu_{2-y}Se$ and $Cu_{2-y}S$. The large *ZT* value for the $Cu_{2-y}Se_{0.5}S_{0.5}$ compounds can be explained by the relatively high quality factor β, which is a measure of the maximum *ZT* at a given temperature [49]

$$\beta = A\frac{\mu_0(m^*/m_e)^{3/2}}{\kappa_L}T^{5/2} \quad ,(3)$$

and

$$A = 2\pi^{3/2}e\left(\frac{k_B}{e}\right)^2\left(\frac{2m_ek_B}{h^2}\right)^{3/2} \quad .(4)$$

Here e, k_B, and h are the electron charge, Boltzmann constant, and Planck constant, respectively. Thus A is a constant parameter. The quality factor β is just related with several fundamental parameters (μ_0, m^*, κ_L, and T) and it serves as a guideline for searching for good thermoelectric materials. As presented in Fig. 8b, the classic TE compounds used at their respective application temperatures usually have β values less than one [49]. Due to the outstanding electrical transports and ultralow lattice thermal conductivity, a large β value of 1.25 is achieved for $Cu_{2-y}Se_{0.5}S_{0.5}$, which is much higher than those of many classic TE compounds including $Cu_{2-y}Se$ and $Cu_{2-y}S$.

4. Conclusion

To sum up, we have successfully synthesized a series of $Cu_{2-y}Se_{0.5}S_{0.5}$ solid solutions and systematically studied the crystal structure, electrical and thermal transport, and thermoelectric performance. At room temperature, $Cu_{2-y}Se_{0.5}S_{0.5}$ ($y \leqslant 0.06$) is comprised of a mixture of hexagonal and cubic phases, but all phases transform into a single cubic phase after the phase transitions. Very special and unique hierarchical microstructure is observed in $Cu_{2-y}Se_{0.5}S_{0.5}$, including polymorph, nano-domains, and modulated structures. They can significantly diminish the lattice thermal conductivity through multiple phonon scattering mechanisms, leading to a low glass-like thermal conductivity. The liquid-like copper ions at high temperature not only strongly scatter lattice phonons but also diminish part of the heat capacity, leading to the strong PLEC effect. By combing the extraordinarily low speed of sound, an overall ultralow lattice thermal conductivity with values around 0.3-0.4 W m^{-1} K^{-1} is observed in $Cu_{2-y}Se_{0.5}S_{0.5}$, which is similar to the value in Cu_2S. Furthermore, the electrical transport performance of $Cu_{2-y}Se_{0.5}S_{0.5}$ is hugely improved through changing the native Cu vacancies. High power factors are observed in $Cu_{2-y}Se_{0.5}S_{0.5,}$ which is better than $Cu_{2-y}S$ and $Cu_{2-y}Se$ due to its relatively high weighted mobility. In consequence, a large quality factor β and thus a high ZT value of 2.3 is achieved at 1000 K for $Cu_{1.94}Se_{0.5}S_{0.5}$, which is greater than the maximum ZTs in $Cu_{2-y}Se$ and $Cu_{2-y}S$ and are among the highest values in bulk thermoelectric materials.

Acknowledgements

We thanks Prof. G. Jeffrey Snyder and Prof. Jihui Yang for helpful discussions. This work was supported by National Basic Research Program of China (973-program) under Project No. 2013CB632501, National Natural Science Foundation of China (NSFC) under the No. 51472262, Key Research Program of Chinese Academy of Sciences (Grant No. KGZD-EW-T06), International S&T Cooperation Program of China (2015DFA51050), and Shanghai Government (15JC1400301). This work was supported by the Danish National Research Foundation (Centre for Materials Crystallography, DNRF93). ABB thanks the SINO Danish Center for funding. We gratefully acknowledge the RIKEN Harima institute for beam time at BL44B2 at the SPring-8 synchrotron facility.

References

[1] W.G. Zeier, A. Zevalkink, Z.M. Gibbs, G. Hautier, M.G. Kanatzidis, G.J. Snyder, Thinking Like a Chemist: Intuition in Thermoelectric Materials, Angew. Chem. Int. Ed. 55 (2016) 6826-6841.

[2] X. Shi, L. Chen, C. Uher, Recent advances in high-performance bulk thermoelectric materials, Int. Mater. Rev. 61 (2016) 379-415.

[3] J.P. Heremans, V. Jovovic, E.S. Toberer, A. Saramat, K. Kurosaki, A. Charoenphakdee, S. Yamanaka, G.J. Snyder, Enhancement of thermoelectric efficiency in PbTe by distortion of the electronic density of states, Science 321 (2008) 554-557.

[4] J.R. Sootsman, D.Y. Chung, M.G. Kanatzidis, New and old concepts in thermoelectric materials, Angew. Chem. Int. Ed. 48 (2009) 8616-8639.

[5] J. Yang, L. Xi, W. Qiu, L. Wu, X. Shi, L. Chen, J. Yang, W. Zhang, C. Uher, D.J. Singh, On the tuning of electrical and thermal transport in thermoelectrics: an integrated theory-experiment perspective, npj Comput. Mater. 2 (2016) 15015.

[6] C. Xiao, Z. Li, K. Li, P. Huang, Y. Xie, Decoupling Interrelated Parameters for Designing High Performance Thermoelectric Materials, Accounts Chem. Res. 47 (2014) 1287-1295.

[7] S.I. Kim, K.H. Lee, H.A. Mun, H.S. Kim, S.W. Hwang, J.W. Roh, D.J. Yang, W.H. Shin, X.S. Li, Y.H. Lee, Dense dislocation arrays embedded in grain boundaries for high-performance bulk thermoelectrics, Science 348 (2015) 109-114.

[8] J. Yang, H.-L. Yip, A.K.Y. Jen, Rational Design of Advanced Thermoelectric Materials, Adv. Energy Mater. 3 (2013) 549-565.

[9] J.F. Li, W.S. Liu, L.D. Zhao, M. Zhou, High-performance nanostructured thermoelectric materials, NPG Asia Mater. 2 (2010) 152-158.

[10] M. Zebarjadi, K. Esfarjani, M. Dresselhaus, Z. Ren, G. Chen, Perspectives on thermoelectrics: from fundamentals to device applications, Energy Environ. Sci. 5 (2012) 5147-5162.

[11] X. Shi, L. Chen, Thermoelectric materials step up, Nat. Mater. 15 (2016) 691-692.

[12] H. Liu, X. Shi, F. Xu, L. Zhang, W. Zhang, L. Chen, Q. Li, C. Uher, T. Day, G.J.

Snyder, Copper ion liquid-like thermoelectrics, Nat. Mater. 11 (2012) 422-425.

[13] Y. He, T. Day, T. Zhang, H. Liu, X. Shi, L. Chen, G.J. Snyder, High Thermoelectric Performance in Non-Toxic Earth-Abundant Copper Sulfide, Adv. Mater. 26 (2014) 3974-3978.

[14] P. Qiu, X. Shi, L. Chen, Cu-based thermoelectric materials, Energy Storage Mater. 3 (2016) 85-97.

[15] B. Yu, W. Liu, S. Chen, H. Wang, H. Wang, G. Chen, Z. Ren, Thermoelectric properties of copper selenide with ordered selenium layer and disordered copper layer, Nano Energy, 1 (2012) 472-478.

[16] F.F. Aliev, M.B. Jafarov, V.I. Eminova, Thermoelectric Figure of merit of Ag_2Se with Ag and Se excess, Semiconductors 43 (2009) 977-979.

[17] P. Qiu, T. Zhang, Y. Qiu, X. Shi, L. Chen, Sulfide bornite thermoelectric material: a natural mineral with ultralow thermal conductivity, Energy Environ. Sci. 7 (2014) 4000-4006.

[18] K.S. Weldert, W.G. Zeier, T.W. Day, M. Panthofer, G.J. Snyder, W. Tremel, Thermoelectric transport in Cu_7PSe_6 with high copper ionic mobility, J. Am. Chem. Soc. 136 (2014) 12035-12040.

[19] B. Gahtori, S. Bathula, K. Tyagi, M. Jayasimhadri, A.K. Srivastava, S. Singh, R.C. Budhani, A. Dhar, Giant enhancement in thermoelectric performance of copper selenide by incorporation of different nanoscale dimensional defect features, Nano Energy 13 (2015) 36-46.

[20] L. Zhao, X. Wang, F.Y. Fei, J. Wang, Z. Cheng, S. Dou, J. Wang, G.J. Snyder,

High thermoelectric and mechanical performance in highly dense $Cu_{2-x}S$ bulks prepared by a melt-solidification technique, J. Mater. Chem. A 3 (2015) 9432-9437.

[21] X. Su, F. Fu, Y. Yan, G. Zheng, T. Liang, Q. Zhang, X. Cheng, D. Yang, H. Chi, X. Tang, Q. Zhang, C. Uher, Self-propagating high-temperature synthesis for compound thermoelectrics and new criterion for combustion processing, Nat. Commun. 5 (2014) 4908.

[22] S.D. Kang, J. Pohls, U.Aydemir, P. Qiu, C.C. Stoumpos, M.A. White, X. Shi, L. Chen, M.G. Kanatzidis, G.J. Snyder, Enhanced stability and thermoelectric figure-of-merit in copper selenide by lithium doping, Mater. Tod. Phy. X (2017) accepted.

[23] L.L. Zhao, X.L. Wang, J.Y. Wang, Z.X. Cheng, S.X. Dou, J. Wang, L.Q. Liu, Superior intrinsic thermoelectric performance with zT of 1.8 in single-crystal and melt-quenched highly dense $Cu_{(2-x)}Se$ bulks, Sci. Rep. 5 (2015) 7671.

[24] L. Yang, Z.G. Chen, G. Han, M. Hong, Y. Zou, J. Zou, High-performance thermoelectric Cu_2Se nanoplates through nanostructure engineering, Nano Energy 16 (2015) 367-374.

[25] Y. He, T. Zhang, X. Shi, S. H. Wei, L. Chen, High thermoelectric performance in copper telluride, NPG Asia Mater. 7 (2015) e210.

[26] E. Eikeland, A. B. Blichfeld, K. A. Borup, K. Zhao, J. Overgaard, X. Shi, L. Chen, B. B. Iversen, The atomic scale origin of the zT enhancing phase transition in thermoelectric $Cu_{2-x}Se$, IUCr-J 2017, submitted.

[27] S.D. Kang, S.A. Danilkin, U. Aydemir, M. Avdeev, A. Studer, G.J. Snyder, Apparent critical phenomena in the superionic phase transition of $Cu_{2-x}Se$, New J. Phys. 18 (2016) 013024.

[28] D. Chakrabarti, D. Laughlin, The Cu-S (copper-sulfur) system, Bull. Alloy Phase Diagrams 4 (1983) 254-271.

[29] S.-y. Miyatani, S. Mori, M. Yanagihara, Phase Diagram and Electrical Properties of $Cu_{2-\delta}Te$, J. Phys. Soc. Jpn. 47 (1979) 1152-1158.

[30] Y. He, P. Lu, X. Shi, F. Xu, T. Zhang, G.J. Snyder, C. Uher, L. Chen, Ultrahigh Thermoelectric Performance in Mosaic Crystals, Adv. Mater. 27 (2015) 3639-3644.

[31] K. Kato, H. Tanaka, Visualizing charge densities and electrostatic potentials in materials by synchrotron X-ray powder diffraction, Advances in Physics: X 1 (2016) 55-80.

[32] B. Jiang, P. Qiu, E. Eikeland, H. Chen, Q. Song, D. Ren, T. Zhang, J. Yang, B.B. Iversen, X. Shi, Cu_8GeSe_6-based thermoelectric materials with argyrodite structure, J. Mater. Chem. C (2016).

[33] W. Qiu, P. Lu, X. Yuan, F. Xu, L. Wu, X. Ke, H. Liu, J. Yang, X. Shi, L. Chen, J. Yang, W. Zhang, Structure family and polymorphous phase transition in the compounds with soft sublattice: Cu_2Se as an example, J. Chem. Phys. 144 (2016) 194502.

[34] C. Frondel, U.B. Marvin, Lonsdaleite, a hexagonal polymorph of diamond, Nature 214 (1967) 587.

[35] A.N. Skomorokhov, D.M. Trots, M. Knapp, N.N. Bickulova, H. Fuess, Structural behaviour of β-$Cu_{2-\delta}Se$ (δ=0, 0.15, 0.25) in dependence on temperature studied by synchrotron powder diffraction, J. Alloy Comp. 421 (2006) 64-71.

[36] P. Qiu, Y. Zhu, Y. Qin, X. Shi, L. Chen, Electrical and thermal transports of binary copper sulfides Cu_xS with x from 1.8 to 1.96, APL Mater. 4 (2016) 104805.

[37] N.A. Alieva, G.G. Guseinov, V.A. Gasymov, Y.I. Alyev, T.R. Mekhtiev, Structural phase transitions of polycrystalline Cu_4SeTe, Inorg. Mater. 51 (2015) 661-664.

[38] J. Baars, G. Brandt, Structural phase transitions in ZnS, J. Phys. Chem. Solids 34 (1973) 905-909.

[39] S. Johnsen, J. He, J. Androulakis, V.P. Dravid, I. Todorov, D.Y. Chung, M.G. Kanatzidis, Nanostructures Boost the Thermoelectric Performance of PbS, J. Am. Chem. Soc. 133 (2011) 3460-3470.

[40] A.F. May, J.-P. Fleurial, G.J. Snyder, Thermoelectric performance of lanthanum telluride produced via mechanical alloying, Phys. Rev. B 78 (2008).

[41] H.J. Goldsmid, Introduction to thermoelectricity, Springer, 2010.

[42] A.F. May, E.S. Toberer, A. Saramat, G.J. Snyder, Characterization and analysis of thermoelectric transport in n-type $Ba_8Ga_{16-x}Ge_{30+x}$, Phys. Rev. B 80 (2009) 125205.

[43] J. Cohn, G. Nolas, V. Fessatidis, T. Metcalf, G. Slack, Glasslike heat conduction

in high-mobility crystalline semiconductors, Phys. Rev. Lett. 82 (1999) 779.

[44] J. Graebner, B. Golding, L. Allen, Phonon localization in glasses, Phys. Rev. B 34 (1986) 5696.

[45] G. Nolas, J. Cohn, G. Slack, Effect of partial void filling on the lattice thermal conductivity of skutterudites, Phys. Rev. B 58 (1998) 164.

[46] J. S. Rhyee, K.H. Lee, S.M. Lee, E. Cho, S.I. Kim, E. Lee, Y.S. Kwon, J.H. Shim, G. Kotliar, Peierls distortion as a route to high thermoelectric performance in $In_4Se_{3-\delta}$ crystals, Nature 459 (2009) 965-968.

[47] K. Trachenko, Heat capacity of liquids: An approach from the solid phase, Phys. Rev. B 78 (2008) 104201.

[48] O. Delaire, A.F. May, M.A. McGuire, W.D. Porter, M.S. Lucas, M.B. Stone, D.L. Abernathy, V.A. Ravi, S.A. Firdosy, G.J. Snyder, Phonon density of states and heat capacity of $La_{3-x}Te_4$, Phys. Rev. B 80 (2009).

[49] H. Wang, Y. Pei, A.D. LaLonde, G.J. Snyder, Material design considerations based on thermoelectric quality factor, in: Thermoelectric Nanomaterials, Springer, 2013, pp. 3-32.

Figure Captions

Fig. 1 (a) Visualization of the crystal structure ($P6_3/mmc$) of $Cu_2Se_{0.5}S_{0.5}$ obtained from single crystal structural solution at 100 K. The blue tetrahedron illustrates the disordered Cu2 sites and the red octahedron the Cu1 sites. The atomic site occupancy is indicated by partial coloring of the atoms. (b) Room temperature powder X-ray diffraction patterns for $Cu_{2-y}Se_{0.5}S_{0.5}$ (x = 0, 0.03, 0.04, 0.05, 0.06 and 0.15) samples ground from the annealed ingots. (c) High temperature synchrotron powder X-ray diffraction patterns for $Cu_2Se_{0.5}S_{0.5}$ measured from 300 K to 1000 K.

Fig. 2 (a) Phase map of $Cu_{1.94}Se_{0.5}S_{0.5}$ obtained from electron backscatter diffraction (EBSD) measurements. The red grains are identified as the hexagonal phases while the blue grains are for the cubic phases. (b) Grain size distribution histograms of hexagonal phases and cubic phases in $Cu_{1.94}Se_{0.5}S_{0.5}$ sample. (c) In-situ elemental energy-dispersive X-ray spectroscopy (EDS) mapping in $Cu_{1.94}Se_{0.5}S_{0.5}$.

Fig. 3 Microstructures of the hexagonal phases in $Cu_2Se_{0.5}S_{0.5}$ and the cubic phases in $Cu_{1.94}Se_{0.5}S_{0.5}$. (a) Low-magnification transmission electron microscope (TEM) image with the corresponding selected area electron diffraction (SAED) pattern for the hexagonal phases in $Cu_2Se_{0.5}S_{0.5}$. (b) High-magnification TEM image and (c) High angle annular dark field (HAADF) image for the hexagonal phases in $Cu_2Se_{0.5}S_{0.5}$. (d) Low-magnification transmission electron microscope (TEM) image with the corresponding SAED patterns for primitive (left) and modulated (right) structures of

cubic phases in $Cu_{1.94}Se_{0.5}S_{0.5}$. (e) HAADF images of the interface between the primitive and modulated phases. (f) HAADF image for the modulated cubic phases in $Cu_{1.94}Se_{0.5}S_{0.5}$.

Fig. 4 Temperature dependence of (a) electrical resistivity ρ, (b) Seebeck coefficient S, (c) power factor PF, (d) total thermal conductivity κ, (e) lattice thermal conductivity κ_L and (f) TE Figure of merit ZT for $Cu_{2-y}Se_{0.5}S_{0.5}$ (y = 0, 0.03, 0.04, 0.05 and 0.06). The data of Cu_2Se and Cu_2S are also included for comparison [12, 13].

Fig. 5 Electrical transport properties of $Cu_{2-y}Se_{0.5}S_{0.5}$ as a function of copper vacancies y at 300 K. (a) Hole carrier concentration p, (b) carrier mobility μ_H, (c) electrical resistivity ρ, and (d) Seebeck coefficient S. The data of $Cu_{2-y}Se$ and $Cu_{2-y}S$ are also included for comparison [12, 13].

Fig. 6 (a) S and (b) PF as a function of Hall carrier concentration at 1000 K. Here the hold concentration at 300 K is used. The symbols are from the experimental data and the curves are calculated based on the single parabolic band (SPB) model. The data of $Cu_{2-y}Se$ and $Cu_{2-y}S$ are also included for comparison [12, 13].

Fig. 7 Thermal transport properties of $Cu_{2-y}Se_{0.5}S_{0.5}$. (a) Lattice thermal conductivity κ_L as a function of copper vacancy y at 300 K and 1000 K. (b) Temperature dependency of κ_L at low temperature (2-300K). (c) Longitudinal speed of sound v_l and

transverse speed of sound v_t for $Cu_{2-y}Se_{0.5}S_{0.5}$ (y = 0, 0.03 and 0.06). The data of $Cu_{2-y}Se$ and $Cu_{2-y}S$ are also included for comparison [12, 13]. (d) Temperature dependency of the heat capacity for $Cu_{2-y}Se_{0.5}S_{0.5}$ at constant pressure (C_p) and volume (C_v). The theoretical value (Dulong-Petit) of C_v at high temperature is $3Nk_B$ in a solid crystal (green dashed curve). The lowest theoretical C_v value in a liquid is $2Nk_B$ (yellow dashed curve).

Fig. 8 (a) *ZT* as a function of Hall carrier concentration p at 1000 K. The symbols are for experimental data and the curves are calculated from the single parabolic band (SPB) model. The data of $Cu_{2-y}Se$ and $Cu_{2-y}S$ are also included for comparison [12, 13]. (b) Quality factor β for $Cu_{2-y}Se_{0.5}S_{0.5}$ and a few other classic thermoelectric compounds at their respective application temperatures [49].

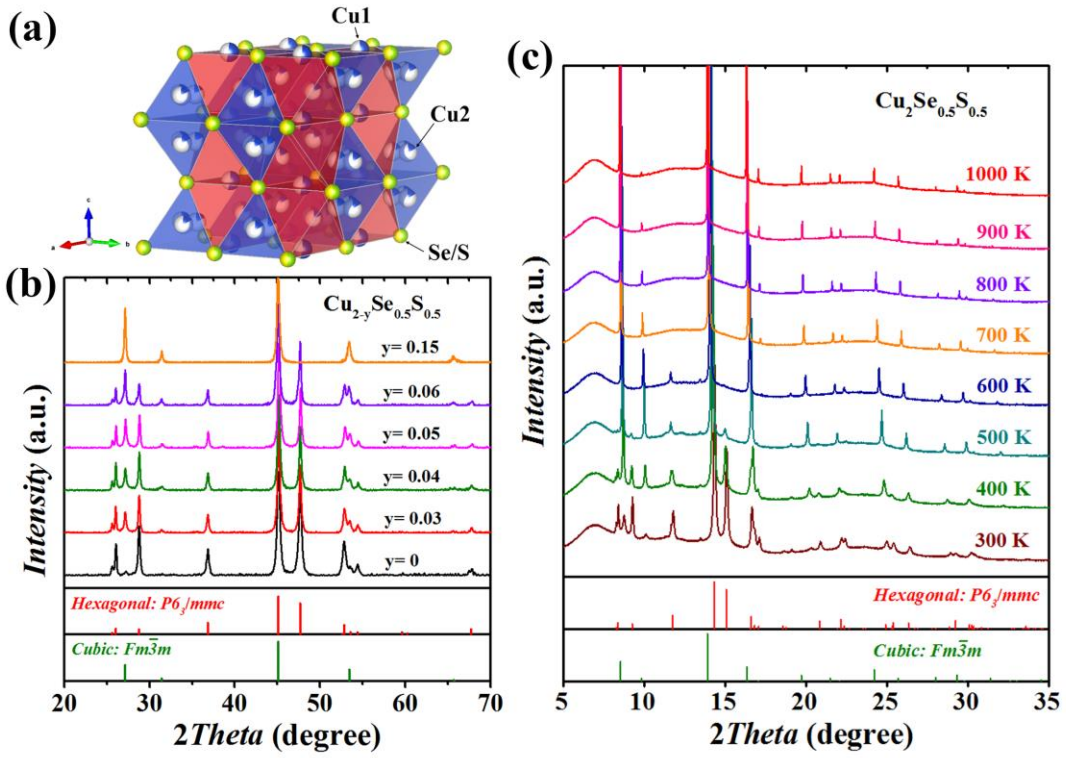

Fig. 1. (a) Visualization of the crystal structure ($P6_3/mmc$) of $Cu_2Se_{0.5}S_{0.5}$ obtained from single crystal structural solution at 100 K. The blue tetrahedron illustrates the disordered Cu2 sites and the red octahedron the Cu1 sites. The atomic site occupancy is indicated by partial coloring of the atoms. (b) Room temperature powder X-ray diffraction patterns for $Cu_{2-y}Se_{0.5}S_{0.5}$ (x = 0, 0.03, 0.04, 0.05, 0.06, and 0.15) samples ground from the annealed ingots. (c) High temperature synchrotron powder X-ray diffraction patterns for $Cu_2Se_{0.5}S_{0.5}$ measured from 300 K to 1000 K.

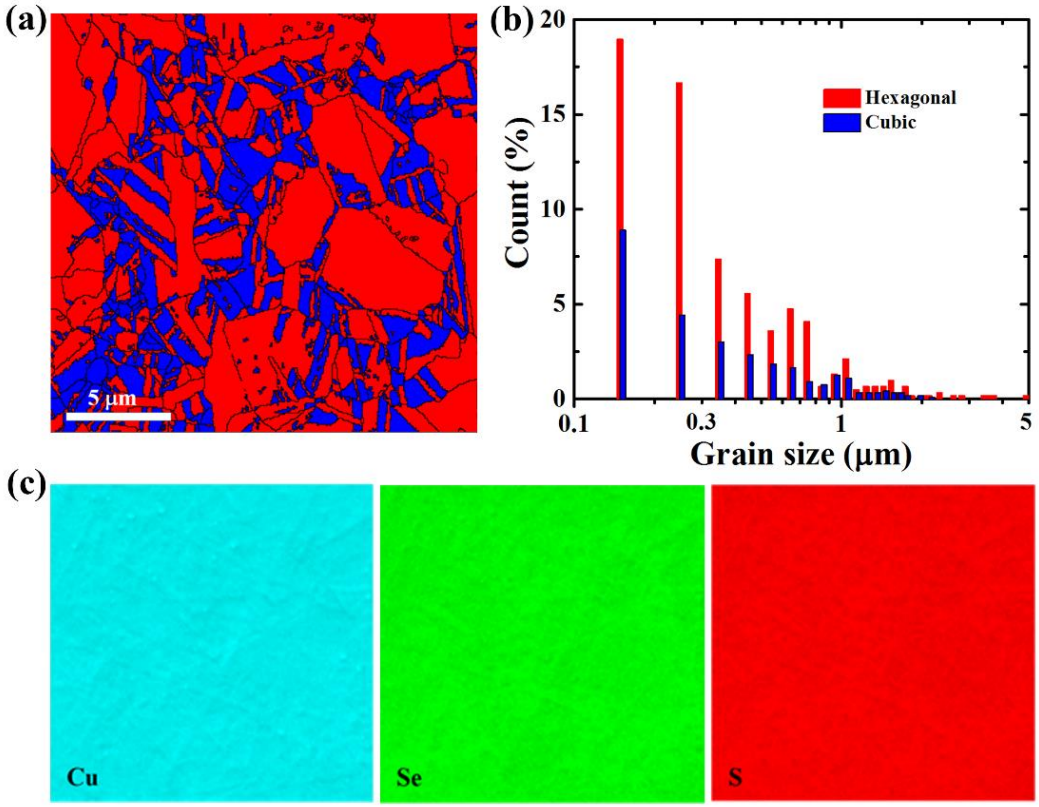

Fig. 2. (a) Phase map of $Cu_{1.94}Se_{0.5}S_{0.5}$ obtained from electron backscatter diffraction (EBSD) measurements. The red grains are identified as the hexagonal phases while the blue grains are for the cubic phases. (b) Grain size distribution histograms of hexagonal phases and cubic phases in $Cu_{1.94}Se_{0.5}S_{0.5}$ sample. (c) In-situ elemental energy-dispersive X-ray spectroscopy (EDS) mapping in $Cu_{1.94}Se_{0.5}S_{0.5}$.

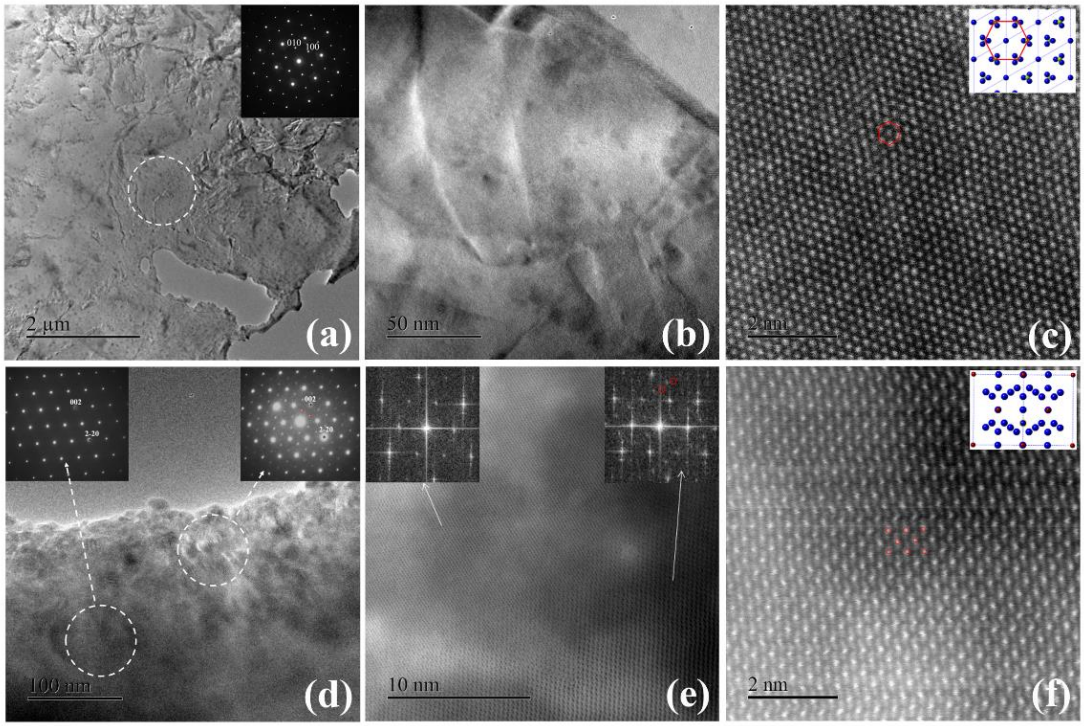

Fig. 3. Microstructures of the hexagonal phases in $Cu_2Se_{0.5}S_{0.5}$ and the cubic phases in $Cu_{1.94}Se_{0.5}S_{0.5}$. (a) Low-magnification transmission electron microscope (TEM) image with the corresponding selected area electron diffraction (SAED) pattern for the hexagonal phases in $Cu_2Se_{0.5}S_{0.5}$. (b) High-magnification TEM image and (c) High angle annular dark field (HAADF) image for the hexagonal phases in $Cu_2Se_{0.5}S_{0.5}$. (d) Low-magnification transmission electron microscope (TEM) image with the corresponding SAED patterns for primitive (left) and modulated (right) structures of cubic phases in $Cu_{1.94}Se_{0.5}S_{0.5}$. (e) HAADF images of the interface between the primitive and modulated phases. (f) HAADF image for the modulated cubic phases in $Cu_{1.94}Se_{0.5}S_{0.5}$.

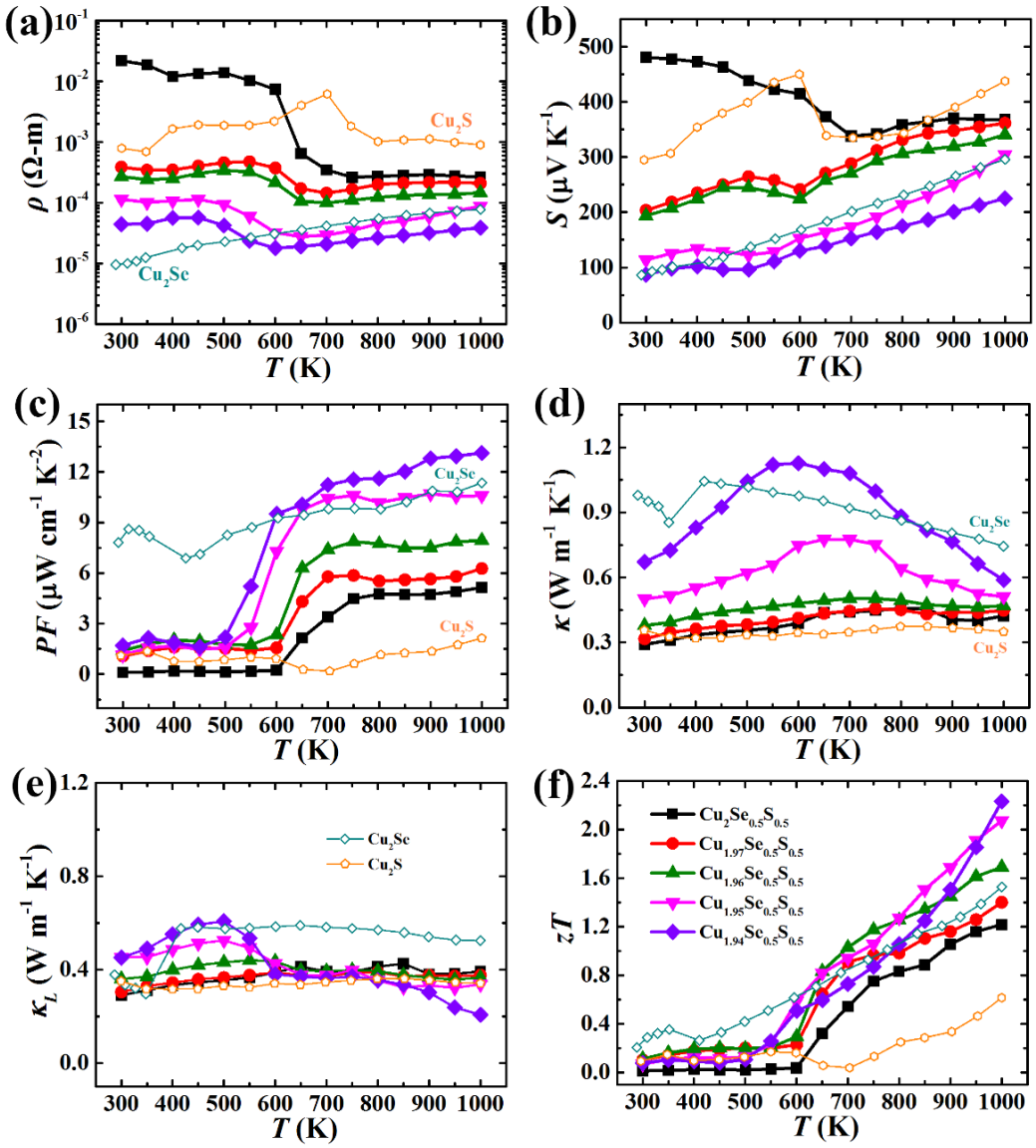

Fig. 4. Temperature dependence of (a) electrical resistivity ρ, (b) Seebeck coefficient S, (c) power factor PF, (d) total thermal conductivity κ, (e) lattice thermal conductivity κ_L and (f) TE Figure of merit ZT for $Cu_{2-y}Se_{0.5}S_{0.5}$ (y = 0, 0.03, 0.04, 0.05, and 0.06). The data of Cu_2Se and Cu_2S are also included for comparison [12, 13].

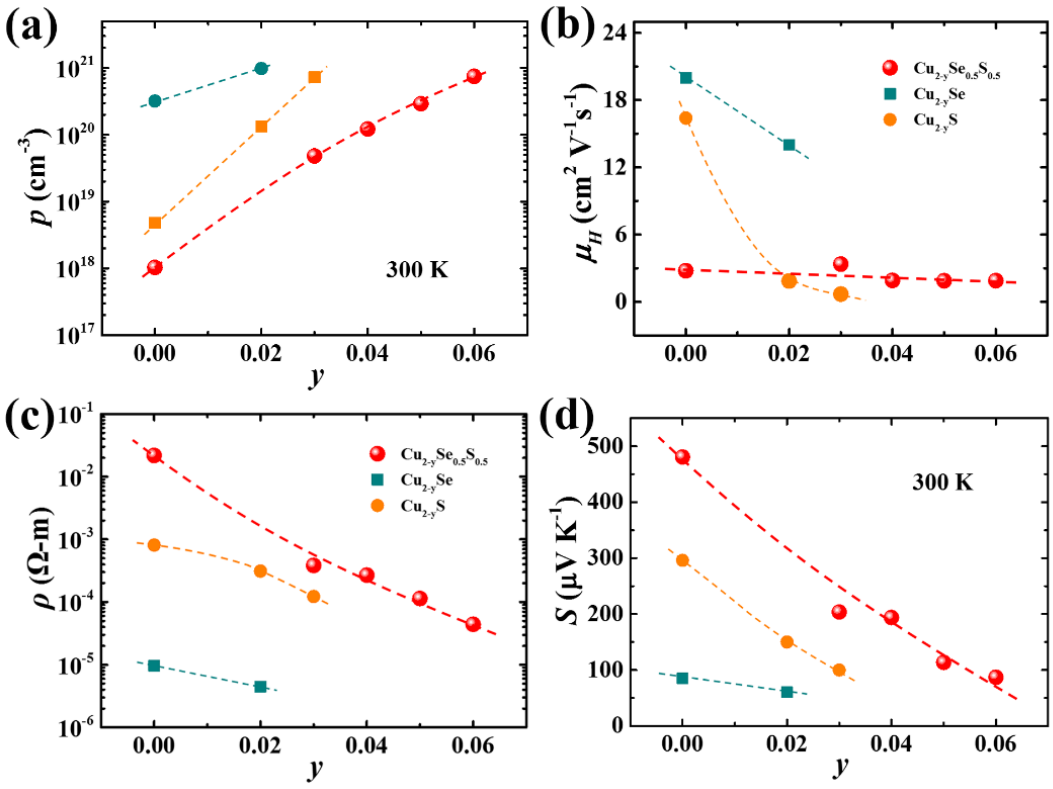

Fig. 5. Electrical transport properties of $Cu_{2-y}Se_{0.5}S_{0.5}$ as a function of copper vacancies y at 300 K. (a) Hole carrier concentration p, (b) carrier mobility μ_H, (c) electrical resistivity ρ, and (d) Seebeck coefficient S. The data of $Cu_{2-y}Se$ and $Cu_{2-y}S$ are also included for comparison [12, 13].

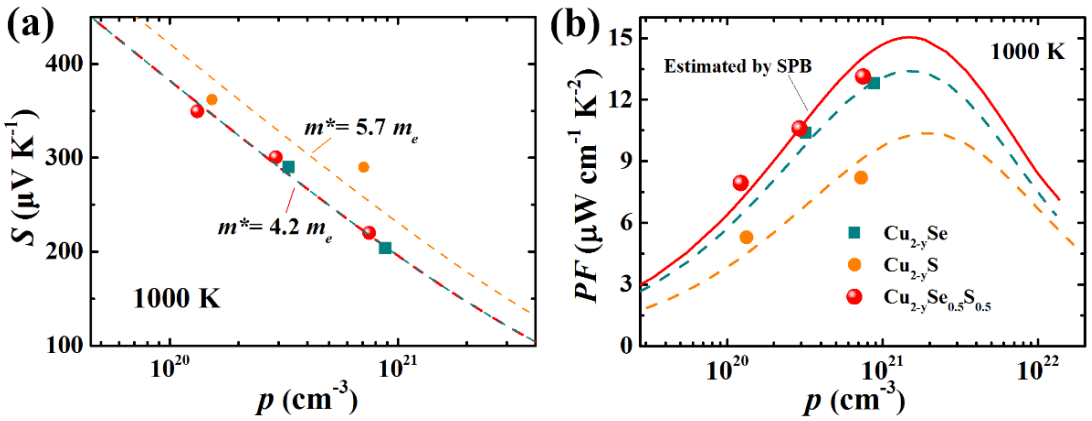

Fig. 6. (a) S and (b) PF as a function of Hall carrier concentration at 1000 K. Here the hold concentration at 300 K is used. The symbols are from the experimental data and

the curves are calculated based on the single parabolic band (SPB) model. The data of $Cu_{2-y}Se$ and $Cu_{2-y}S$ are also included for comparison [12, 13].

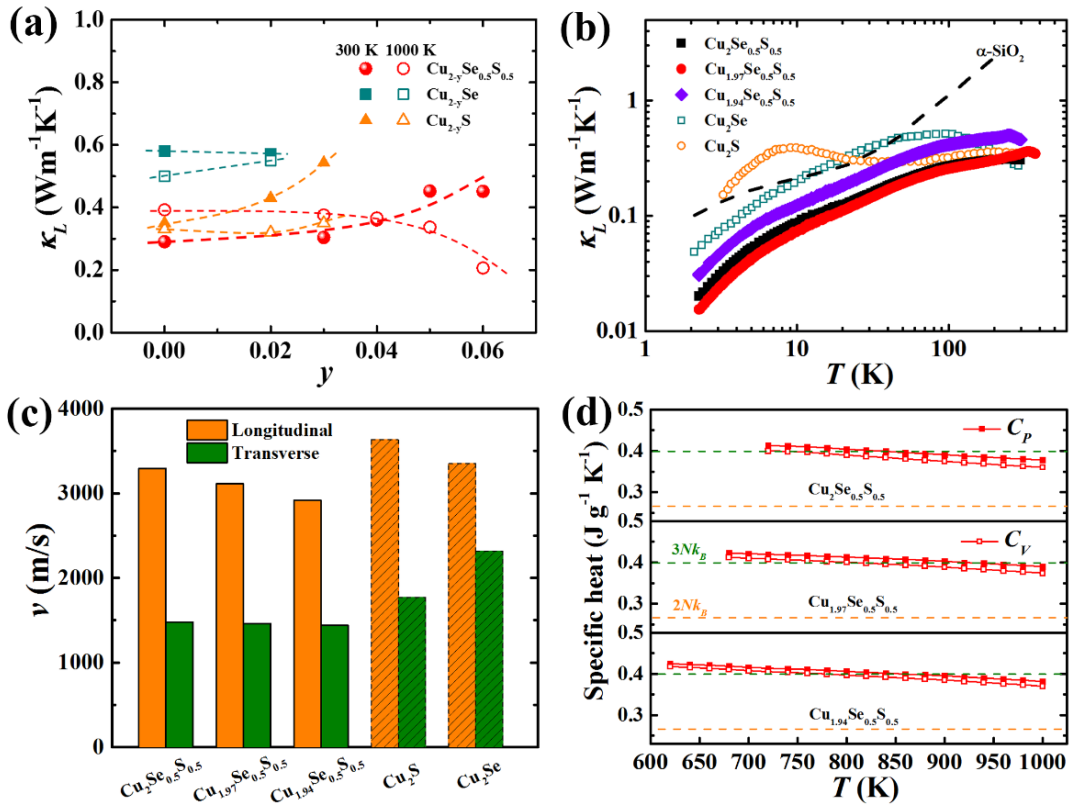

Fig. 7. Thermal transport properties of $Cu_{2-y}Se_{0.5}S_{0.5}$. (a) Lattice thermal conductivity κ_L as a function of copper vacancy y at 300 K and 1000 K. (b) Temperature dependency of κ_L at low temperature (2-300K). (c) Longitudinal speed of sound v_l and transverse speed of sound v_t for $Cu_{2-y}Se_{0.5}S_{0.5}$ (y = 0, 0.03, and 0.06). The data of $Cu_{2-y}Se$ and $Cu_{2-y}S$ are also included for comparison [12, 13]. (d) Temperature dependency of the heat capacity for $Cu_{2-y}Se_{0.5}S_{0.5}$ at constant pressure (C_p) and volume (C_v). The theoretical value (Dulong-Petit) of C_v at high temperature is $3Nk_B$ in a solid crystal (green dashed curve). The lowest theoretical C_v value in a liquid is $2Nk_B$ (yellow dashed curve).

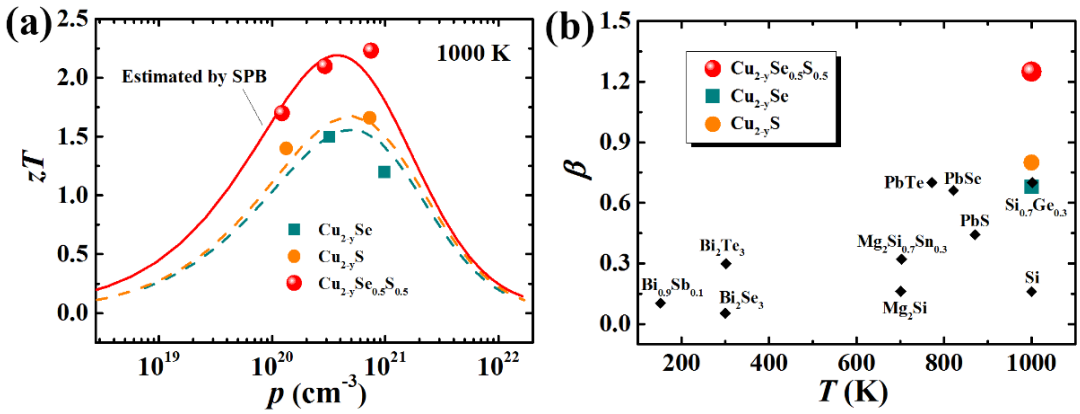

Fig. 8. (a) *ZT* as a function of Hall carrier concentration *p* at 1000 K. The symbols are for experimental data and the curves are calculated from the single parabolic band (SPB) model. The data of $Cu_{2-y}Se$ and $Cu_{2-y}S$ are also included for comparison [12, 13]. (b) Quality factor β for $Cu_{2-y}Se_{0.5}S_{0.5}$ and a few other classic thermoelectric compounds at their respective application temperatures [49].

Table 1. Electronic transport parameters (effective mass m^*, deformation potential Ξ, alloy scattering potential U, mobility parameter μ_0 and quality factor β) and lattice thermal conductivities κ_L of $Cu_{2-y}Se_{0.5}S_{0.5}$, $Cu_{2-y}Se$ and $Cu_{2-y}S$ at 1000 K.

Material	$Cu_{2-y}Se_{0.5}S_{0.5}$	$Cu_{2-y}Se$	$Cu_{2-y}S$
m^* (m_e)	4.2	4.2	5.7
Ξ (eV)	3.0	3.1	3.1
U (eV)	0.05		
μ_0 ($cm^2\ V^{-1}s^{-1}$)	2.4	2.2	1.0
$\mu_0(m^*/m_e)^{3/2}$ ($cm^2\ V^{-1}s^{-1}$)	20.6	18.9	13.6

κ_L (W m^{-1} K^{-1})	0.30	0.51	0.31
β	1.25	0.68	0.80
$p_{opt,\,PF}$ (10^{20} cm^{-3})	15.2	14.9	18.5
$(PF)_{max}$ (1000 K)	15.0	13.4	10.3
$p_{opt,\,ZT}$ (10^{20} cm^{-3})	3.44	4.08	4.83
$(ZT)_{max}$ (1000 K)	2.17	1.54	1.67